Creating Composite Vortex Beams with a Single Geometric Metasurface

Yang Ming, Yuttana Intaravanne, Hammad Ahmed, Mitchell Kenney, Yan-qing Lu, and Xianzhong Chen*

Composite vortex beams (CVBs) have attracted considerable interest recently due to the unique optical properties and potential applications. However, these beams are mainly generated using spatial light modulators, which suffer from large volume, high cost, and limited resolution. Benefiting from the ultrathin nature and unprecedented capability in light manipulation, optical metasurfaces provide a compact platform to perform this task. A metasurface approach to creating these CVBs is proposed and experimentally demonstrated. The design is based on the superposition of multiple circularly polarized vortex beams with different topological charges, which is realized based on a geometric metasurface consisting of metallic nanorods with spatially variant orientations. The effects of the initial phases, amplitude coefficients, incident polarization state, and propagation distance on the generated CVBs, which are in good agreement with the theoretical prediction, are experimentally analyzed. This work has opened a new avenue for engineering CVBs with a minimal footprint, which has promising applications ranging from multiple optical traps to quantum science.

1. Introduction

The nontrivial behaviors of phase give rise to diverse intriguing phenomena, opening up the area of singular optics.[1] Optical vortices (known as singular light beams) have been used in many fields ranging from particle manipulation[2,3] to quantum information[4,5] due to their unique optical properties. The singularity structure of a wavefront plays an important role in the physical properties of vortex beams.[6] Unlike a vortex beam with a single singularity, composite vortices with more elaborate singularity distributions are endowed with enhanced capacity and more flexibility,[7,8] which have promising applications in multiple optical traps,[9] electromagnetically induced transparency,[10] and quantum computation gate.[11] Currently, such composite vortex beams (CVBs) are mainly generated based on spatial light modulators (SLMs),[7,12] which suffer from large volume, high cost, and low resolution. To keep the pace of device miniaturization and system integration, tackling these challenges typically associated with CVBs generation is urgently needed.

Emerging optical metasurfaces have provided unprecedented capabilities to locally manipulate light's phase, amplitude, and polarization at subwavelength scale, leading to the development of novel metasurface devices, including metalenses,[13–16] multifunctional devices,[17–21] polarization-sensitive holograms,[22–25] vortex beam generators,[26–30] and polarization structure generation.[31–33] The ultrathin nature of metasurfaces makes them desirable for miniaturization and integration. Optical metasurfaces have been used to generate vortex beams and realize the superposition of these beams.[34] These demonstrations prove that metasurfaces can be used to create complicated singularity structures based on the superposition of two vortex beams.[34–36] However, the superposition of multiple vortex beams (three or more) is needed to engineer the singularity structure of CVBs, which has not been demonstrated with optical metasurfaces. In addition, unlike SLMs, geometric optical metasurfaces are sensitive to polarization states of the light, providing a new degree of freedom to engineer CVBs.

We propose and experimentally demonstrate a single metasurface for creating these CVBs. Our design is based on the superposition of multiple vortex beams with different combinations

Y. Ming, Y. Intaravanne, H. Ahmed, X. Chen
Institute of Photonics and Quantum Sciences
School of Engineering and Physical Sciences
Heriot-Watt University
Edinburgh EH14 4AS, UK
E-mail: x.chen@hw.ac.uk
Y. Ming
School of Electronic and Information Engineering
Changshu Institute of Technology
Suzhou 215000, China
Y. Ming, Y.-q. Lu
National Laboratory of Solid State Microstructures
College of Engineering and Applied Sciences
Nanjing University
Nanjing 210093, China
M. Kenney
Optics and Photonics Group
Faculty of Engineering
University of Nottingham
University Park, Nottingham NG7 2RD, UK

**ADVANCED
SCIENCE NEWS** _____
www.advancedsciencenews.com

**ADVANCED
MATERIALS**
www.advmat.de

of circular polarizations, which is realized based on a geometric metasurface consisting of metallic nanorods with spatially variant orientations. Unlike previously demonstrated metasurface based superposition of two vortex beams, four vortex beams with different combinations of circular polarizations are involved in our work. The CVBs are experimentally demonstrated and compared with simulation results, which shows that a single metasurface can create and engineer singularity structures. The effects of the initial phases, the amplitude coefficients and the incident polarization states for modulating the singularity structures are analyzed. Our work opens a new avenue for engineering CVBs with a minimal footprint.

2. Results

2.1. Design Principle

Figure 1 shows the schematic of the metasurface approach and the generated CVBs. The metasurface consists of gold nanorods with spatially variant orientations sitting on the glass substrate. Upon the illumination of a circularly polarized light beam, the CVB with the opposite circular polarization state is obtained on the transmission side based on the superposition of four vortex beams with different topological charges (corresponding phase profiles shown at the top inset of Figure 1), which can generate complex singularity structures. The evolution process of intensity profiles of the resultant CVBs along the light propagation direction is expected.

The Laguerre–Gaussian (LG) modes are typically used for optical vortices; these LG modes are mainly characterized by two parameters: l and p, which represent the topological charge and the number of radial nodes, respectively[6]

$$
\begin{aligned}
\text{LG}_{pl} = &\sqrt{\frac{2p!}{\pi(p+|l|)!}} \frac{1}{w(z)} \left[\frac{r\sqrt{2}}{w(z)}\right]^{|l|} \exp\left[\frac{-r^2}{w^2(z)}\right] L_p^{|l|} \left[\frac{2r^2}{w^2(z)}\right] \exp(il\theta) \\
&\times \exp\left[\frac{ikr^2 z}{2(z^2+z_R^2)}\right] \exp\left[-i(2p+|l|+1)\tan^{-1}\left(\frac{z}{z_R}\right)\right]
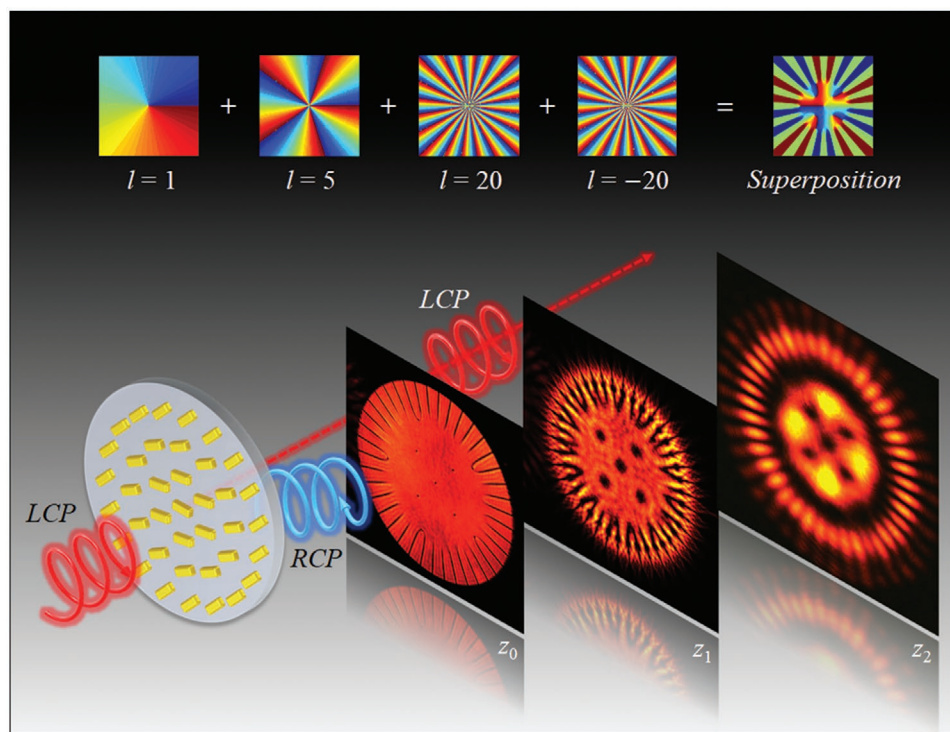\end{aligned}
\tag{1}
$$

where

$$
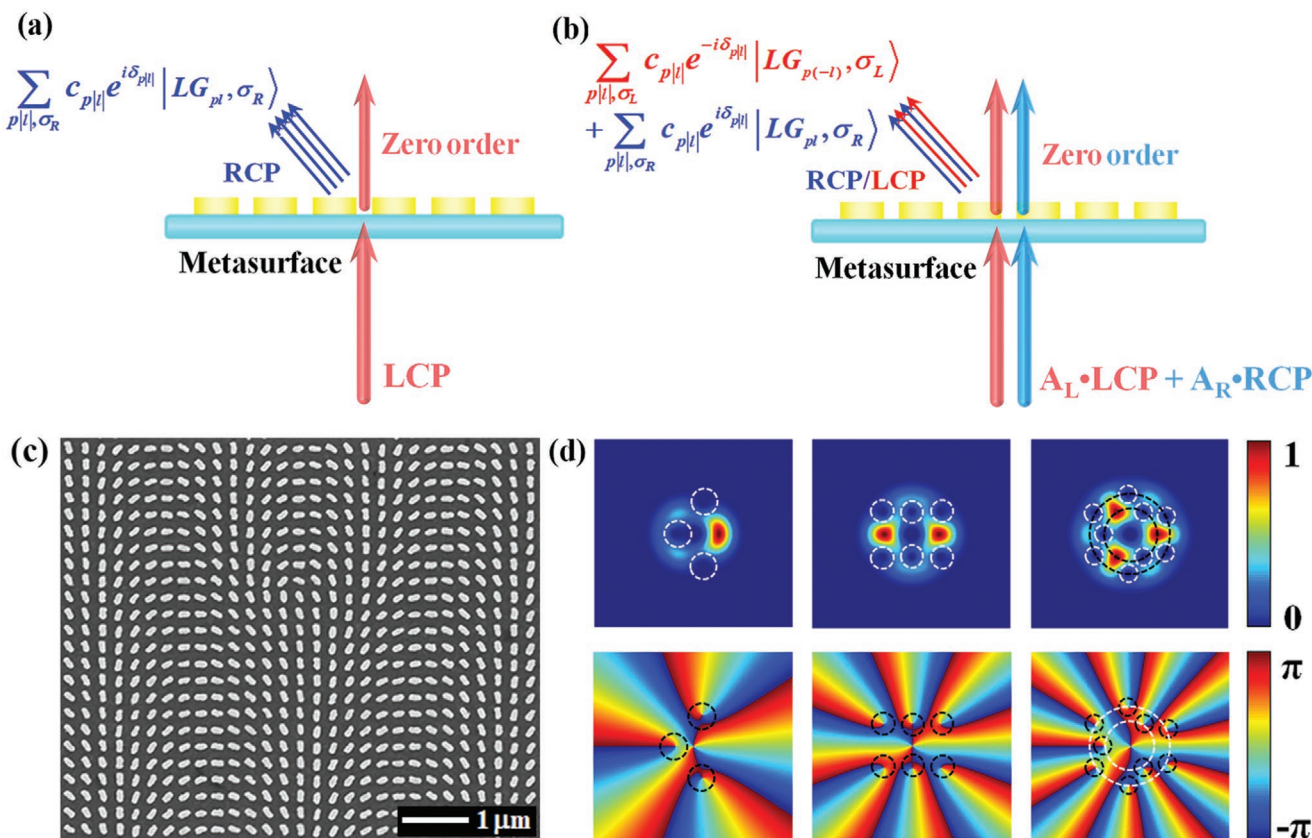w(z) = w_0 \sqrt{1 + \left(\frac{z}{z_R}\right)^2}, z_R = \frac{\pi w_0^2}{\lambda}
\tag{2}
$$

$w(z)$ and w_0 denote the beam radius at z and $z = 0$, respectively. The parameter z_R is the Rayleigh range of Gaussian envelope, and $(2p + |l| +1)\tan^{-1}(z/z_R)$ is the Gouy phase.

The general superposition of multiple LG modes with specific polarization states can be expressed as

$$
\left|\text{LG}\right\rangle_{\text{sup}} = \sum_{pl,\sigma}^{N} c_{pl} e^{i\delta_{pl}} \left|\text{LG}_{pl}, \sigma\right\rangle
\tag{3}
$$

Figure 1. Schematic of proposed approach for CVBs generation using a single metasurface. Under the illumination of LCP light, the CVB with a polarization state of RCP is generated on the transmission side of the metasurface, which consists of gold nanorods with spatially variant orientations. As an example, the design here is based on the superposition of four vortex beams with different topological charges, whose phase profiles are given on the top. Experimental results for the intensity distributions of the resultant CVB in the different observation planes along the light propagation direction are given here. $z_0 = 0.1$ mm, $z_1 = 1.2$ mm, and $z_2 = 30$ mm.

**ADVANCED
SCIENCE NEWS**

www.advancedsciencenews.com

**ADVANCED
MATERIALS**

www.advmat.de

Figure 2. Schematic of the superposition mechanism, fabricated metasurface and simulation results. a) Upon the illumination of a pure LCP light beam, the deflected light forms the CVB with the opposite circular polarization (RCP) through the superposition of LG modes. b) When the input light has an arbitrary polarization state (A_L·LCP + A_R·RCP), the resultant CVB is generated through the superposition of LG modes with different combinations of circular polarization states. c) The SEM image of a fabricated metasurface sample. d) The superposition of three LG beams: $LG_2 + LG_3 + LG_5$, $LG_2 + LG_4 + LG_8$, and $LG_2 + LG_5 + LG_{11}$. The upper row shows the intensity profiles, whose phase profiles are shown in the lower row. The positions of the phase singularities are marked with white dashed circles. Dark regions are observed in the intensity patterns.

where N is the total number of modes for superposition, c_{pl} and δ_{pl} are the amplitude coefficient and the initial phase, respectively, and σ is the circular polarization state.

To experimentally realize the superposition of multiple vortex beams with different combinations of circular polarization states, a geometric metasurface with an off-axis design is used. The schematic of the superposition mechanism is shown in **Figure 2**a,b. The off-axis design can avoid the hassle of the nonconverted part. All gold nanorods have the same dimensions, but with spatially variant orientation angles $\varphi(x,y)$, which are governed by[34]

$$\varphi(x,y) = \frac{1}{2}\arg\left\{\sum_{N}^{j=1} c_j LG_{p_j l_j} \exp\left[i\left(l_j\theta + \Delta\phi_j + \delta_j\right)\right]\right\} \quad (4)$$

where the phase difference $\Delta\phi_j$ between neighboring pixels is defined along the x direction. As shown in Figure 2a, when a left-circularly polarized (LCP) or right-circularly polarized (RCP) light beam shines on the metasurface, the CVB with the opposite circular polarization (RCP or LCP) is generated based on the deflected light through the superposition of multiple LG modes, which are given in Equation (4). Figure 2b exhibits the other case when the input light has an arbitrary polarization

state, which can be decomposed into LCP and RCP components. The resultant CVB is formed by the superposition of LG modes with different circular polarization states.

In the following, we mainly focus on the situation $p = 0$ as it allows for a simple but highly adaptable formation of composite vortices, even for more complicated cases. The metasurface samples are fabricated using the standard electron beam lithography and lift-off process, and the fabrication details are provided in the Experimental Section. A scanning electron microscopy (SEM) image of the fabricated sample is given in Figure 2c. Each nanorod is 215 nm long, 125 nm wide, and 40 nm high. The dimension of each unit cell is 300 × 300 nm². The size of sample is 348 μm × 348 μm. The additional phase difference $\Delta\phi$ between the neighboring pixels along the horizontal direction is set to be $\pi/5$, which can generate a phase gradient for the off-axis design. A supercontinuum laser (NKT Photonics SuperK EXTREME) is used as the light source to characterize the performance of the metasurface device. In our experiment, the wavelength we use is 630 nm. A linear polarizer and a quarter wave plate (QWP) are used to control the polarization state of the incident light. Details of the experimental setup are given in Section S1 (Supporting Information).

**ADVANCED
SCIENCE NEWS**

www.advancedsciencenews.com

**ADVANCED
MATERIALS**

www.advmat.de

2.2. Superposition of LG Beams with Same Circular Polarization State

We first consider the superposition of LG modes with the same circular polarization state. Using more than two vortices for the superposition can substantially improve the manipulation diversity. Therefore, we start to investigate the superposition based on three LG modes.

2.2.1. Superposition of Three LG Beams

The corresponding expression in Equation (3) is

$$|LG\rangle_{\text{sup}} = \frac{1}{\sqrt{c_{l_1}^2 + c_{l_2}^2 + c_{l_3}^2}} \left(c_{l_1} e^{i\delta_1} |LG_{l_1}\rangle + c_{l_2} e^{i\delta_2} |LG_{l_2}\rangle + c_{l_3} e^{i\delta_3} |LG_{l_3}\rangle \right) \quad (5)$$

The subscripts l_1, l_2, and l_3 represent the parameters of three LG modes, respectively.

Several composite modes with different combinations of l_1, l_2, and l_3 at $z = 0$ are initially simulated. The selected combinations include $(l_1, l_2, l_3) = (2, 3, 5)$, $(2, 4, 8)$, and $(2, 5, 11)$, where $c_{l_1} = c_{l_2} = c_{l_3} = 1$ and $\delta_{l_1} = \delta_{l_2} = \delta_{l_3} = 0$. The intensity profiles and phase diagrams are shown in Figure 2d. The phase singularities and corresponding dark spots are denoted by the white and black dashed circles. It can be seen that the third case $LG_2 + LG_5 + LG_{11}$ (Figure 2d) exhibits an intensity profile with a double-concentric Ferris wheel. For the other two cases, owing to the small difference between l_1, l_2, and l_3, the inner and outer wheels are merged. In the case of $LG_2 + LG_3 + LG_5$, there is an overlap between the sole dark spot on the inner wheel and central dark spot. To avoid the overlap, the differences of topological charges of the LG modes for superposition should be large enough.

In addition, the numbers of dark spots on the Ferris wheel ($LG_2 + LG_5 + LG_{11}$) for the inner and outer layers are equal to $|l_2 - l_1|$ and $|l_3 - l_2|$, respectively. Moreover, as marked by the white dashed circles in Figure 2d, each phase singularity corresponds to a dark spot, which is experimentally verified (**Figure 3**a). The first case (a1) exhibits the simulated and measured intensity patterns for the case with $c_{l_1} = c_{l_2} = c_{l_3} = 1$ and $\delta_{l_1} = \delta_{l_2} = \delta_{l_3} = 0$ when the light travels in the free space. Due to the l-dependent Gouy phase during the propagation process, the rotation of intensity patterns in the CVBs is expected, which is experimentally confirmed (see Figure 3b). Detailed explanation of Gouy phase is available in refs. [34,37].

We further consider manipulating the CVBs by changing the initial phase δ_{l_i} and the amplitude coefficient c_{l_i}. Interestingly, the inner and outer wheels can be rotated by controlling δ_{l_i}. Only the inner wheel is rotated counterclockwise with the increase of δ_{l_1} for $\delta_{l_1} > 0$, while the rotation direction is clockwise for $\delta_{l_1} < 0$. In the case $\delta_{l_3} \neq 0$, only the outer wheel is rotated, and its rotation directions for $\delta_{l_3} > 0$ and for $\delta_{l_3} < 0$ are clockwise and counterclockwise, respectively. If $\delta_{l_2} \neq 0$, the inner and outer wheels can be rotated simultaneously with opposite rotation directions. The detailed discussions about $\delta_{l_1} \neq 0$ and $\delta_{l_3} \neq 0$ are included in Sections S2 and S3 (Supporting Information). Here we mainly focus on the last case $\delta_{l_2} \neq 0$. Figure 3c shows the evolution process of singularity distribution, and the rotation angles of the inner and outer wheels

are calculated. The black and blue curves represent the values for the rotation angles of outer wheels (clockwise) and that of the inner wheels (counterclockwise), respectively. When the initial phase is $\pi/3$, a typical intermediate state is formed. The corresponding calculated and experimental intensity profiles are shown in the second case (a2) of Figure 3a. The rotation angles of the inner and outer wheels are $\pi/18$ (counterclockwise) and $\pi/9$ (clockwise), respectively. Three outer dark spots are merged with the inner dark spots to form larger ones. As the initial phase continues to increase, the intensity profile recovers the original pattern with a whole rotation when $\delta_{l_2} = 2\pi/3$.
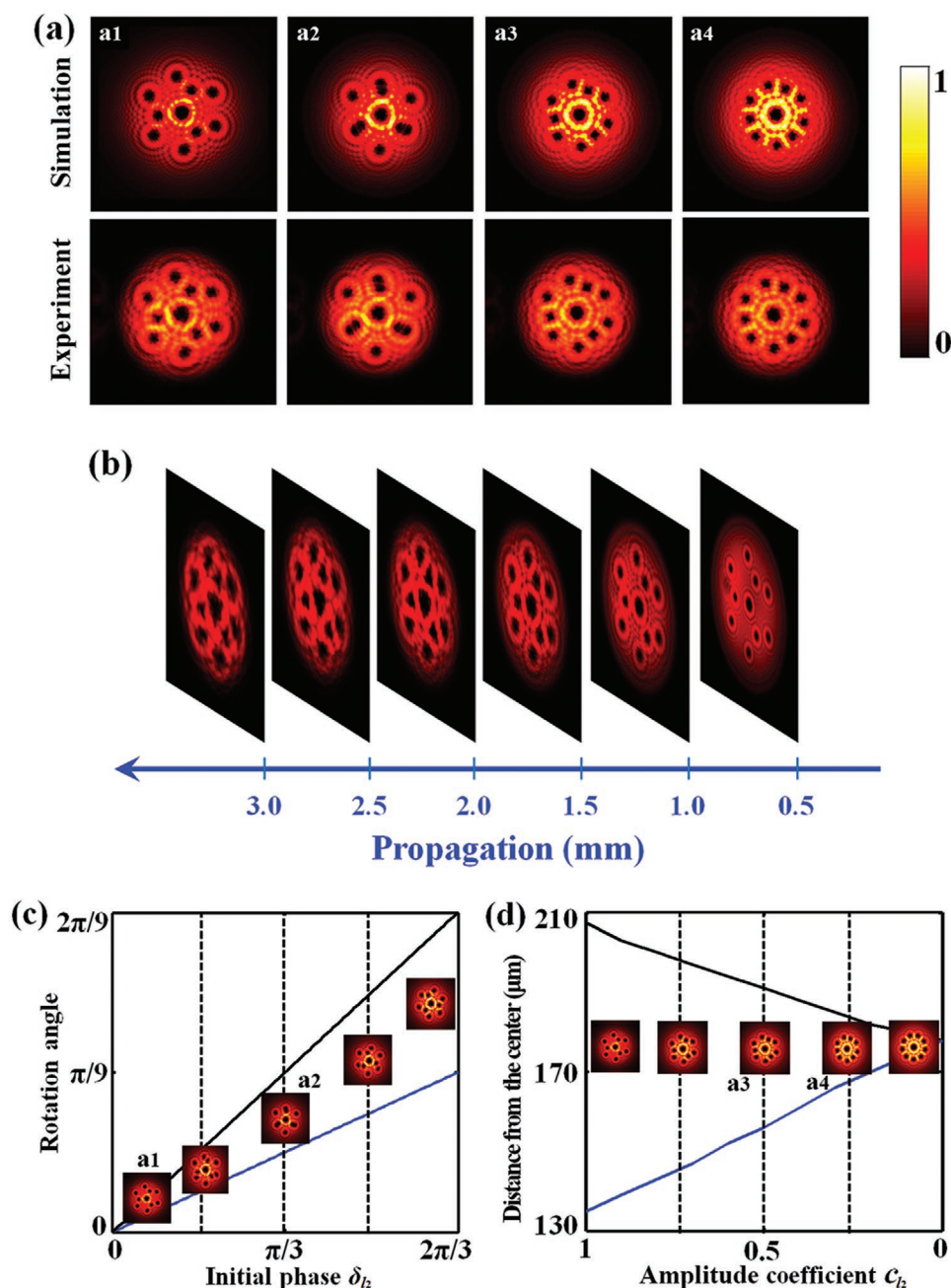
Next, we discuss the different combinations of c_{l_1}, c_{l_2}, and c_{l_3}. The first considered case is $c_{l_1} = c_{l_3} = 1$ and $c_{l_2} < 1$. Figure 3d shows the corresponding evolution process. We can observe a clear trend towards the superposition of $LG_2 + LG_{11}$, which is due to the percentage of LG_5 drops along with c_{l_2}. The black and blue curves represent the calculated radii of outer and inner wheels, respectively. With the decrease of amplitude coefficient c_{l_2}, the results show that the radius of outer wheel becomes smaller, while the radius of the inner wheel becomes larger. When c_{l_2} vanishes, the two radii are equal since the LG_5 component for the superposition is thoroughly removed. Two typical intermediate states for $c_{l_2} = 0.5$ and $c_{l_2} = 0.25$ are shown in Figure 3a (a3 and a4). If c_{l_1} or c_{l_3} decreases while the other two parameters are equal to 1, the composite mode varies towards the superposition of the other two LG modes. In contrast, if one of the three parameters becomes larger, the composite beam approaches the corresponding LG mode.

The experimental measurement of the propagation effect of the CVBs with varying initial phase and amplitude coefficient is also provided in Section S4 (Supporting Information).

2.2.2. Superposition of Four LG Beams

The superposition of four LG modes is divided into two categories: direct superposition of four modes and a combination of two mode superposition. For the first category, we select the superposition $LG_2 + LG_5 + LG_{11} + LG_{23}$, which is expected to generate a CVB with an intensity profile of a triple-concentric Ferris wheel. The simulation and experiment patterns are given in the middle and right columns in **Figure 4**a. The numbers of dark spots on the three concentric circles of the Ferris wheel are equal to $|l_2 - l_1|$, $|l_3 - l_2|$, and $|l_4 - l_3|$, for inner, middle, and outer circles, respectively. Each dark spot corresponds to a phase singularity, as shown in the phase profile (Figure 4a left). The Fourier diffraction theory is used to calculate the evolution of light intensity distribution behind the metasurface.[38] The simulation results show minor deviations from the perfect rotational symmetry of pattern, which are related to the grid size used for the calculations. Taking smaller grid size can help reducing the noise.

For the second category, we choose the LG mode superposition of $LG_1 + LG_5 + LG_{20} + LG_{-20}$. As shown in Figure 4b, both the intensity and phase profiles have two sections, corresponding to the combination of two pairs of LG mode superposition, i.e., $LG_1 + LG_5$ and $LG_{20} + LG_{-20}$. Unlike the previous case, the intensity profile here has a sunflower-like shape, and the number of outer ray florets is equal to twice the value of $|l_3|$ or $|l_4|$. Besides, to clearly separate the inner

**ADVANCED
SCIENCE NEWS**

www.advancedsciencenews.com
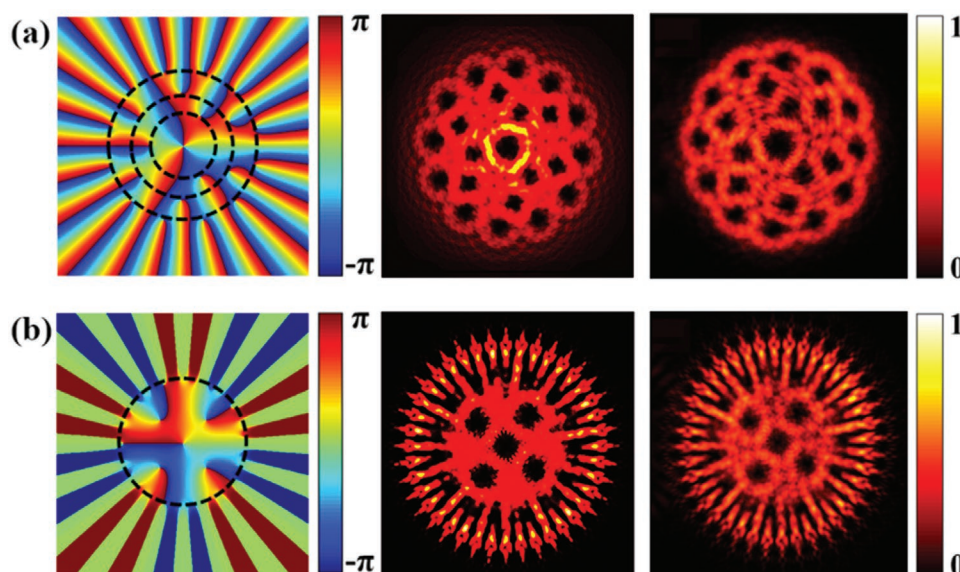
**ADVANCED
MATERIALS**

www.advmat.de

Figure 3. Superposition of three LG modes with the same circular polarization states for the CVBs generation. a) Effects of the initial phase and the amplitude coefficient on the intensity profiles of CVBs. The calculated (top) and measured patterns (bottom). b) The evolution process of the intensity patterns along the propagation direction. c) The effect of initial phase δ_{l_2} on the singularity distribution. The black and blue curves represent the values for the rotation angles of outer wheels (clockwise) and that of the inner wheels (counterclockwise), respectively. d) Effect of the amplitude coefficient c_{l_2} on the generated CVBs. The composite mode varies toward the superposition of $LG_2 + LG_{11}$.

and outer concentric sections, the difference between $|l_2|$ and $|l_3|$ (or $|l_4|$) should be large enough. The inner section of the phase profile also possesses phase singularities, but the outer section exhibits singular lines, leading to the generation of the ray florets. The evolution of the transverse beam intensity along the light propagation is provided by gradually changing the observation plane (Movie S1, Supporting Information).

2.3. Superposition of four LG Modes with Different Circular Polarizations

To demonstrate more nontrivial CVBs, we also investigate the superposition of four LG modes with different combinations of circular polarization states. The case of $LG_1 \hat{e}_R + LG_{-1} \hat{e}_L + LG_7 \hat{e}_R + LG_{-7} \hat{e}_L$ is demonstrated in detail. The denotations $\hat{e}_R$ and $\hat{e}_L$ represent the RCP and LCP

2109714 (5 of 9)

**ADVANCED
SCIENCE NEWS**

www.advancedsciencenews.com

**ADVANCED
MATERIALS**

www.advmat.de

Figure 4. Superposition of four LG modes with the same circular polarization for generating CVBs. The phase profiles (left), simulated intensity profiles (middle), and measured intensity profiles (right) are provided for $LG_2 + LG_5 + LG_{11} + LG_{23}$ (a) and $LG_1 + LG_5 + LG_{20} + LG_{-20}$ (b). The phase singularities are located on the dashed circles.

bases, respectively. A linearly polarized light can be decomposed into two circular polarization states with equal components. Upon the illumination of the incident light with linear polarization, the simulation and experiment results are given in the first and second rows (**Figure 5**a), respectively. The red double arrows show the transmission axes of the linear polarizer. The transmission axis of the analyser is fixed along the vertical direction. The dark gaps in the middle of the intensity patterns clearly show the nature of the vector beam. The resultant CVB can be modulated by controlling the polarization state of input light. Effect of different polarizations states on the simulation and experiment results are given in Figure 5b. The fast axis of the quarter wave plate and the transmission axis of the analyser are fixed along the horizontal and vertical directions, respectively. The polarization states of the incident light are changed by controlling the transmission axes of the first linear polarizer. Both the calculated and measured intensity patterns for the incident light with the circular polarizations (RCP and LCP) show a simple "flower" shape. Since an elliptical polarization state is the intermediate state between circular and linear polarization states, the intensity profile for the elliptical polarization state appears to be the combination of the intensity distributions for the two polarization states. To further demonstrate the influence of input polarization on the resultant CVBs, the simulation and experiment results of another case $LG_2 \hat{e}_R + LG_{-2} \hat{e}_L + LG_6 \hat{e}_R + LG_{-6} \hat{e}_L$ are included in Section S5 in the Supporting Information. Our approach is very robust. Apart from the two pairs of vortex beams superposition with opposite topological charges, the design method can also be used for the superposition of arbitrary combination of vortex beams with different circular polarizations. More simulation results are provided in Section S6 (Supporting Information).

3. Discussion

As a branch of modern optics, singular optics involves many effects associated with the phase singularities in wave fronts, exhibiting some unique features (e.g., OAM) absent in light fields with smooth wave fronts. Optical metasurfaces are ultrathin inhomogeneous media with planar nanostructures that can realize spin–orbit interaction in a desirable manner.[39] Unlike the complex amplitude superposition of composite optical field for the development of unusual metalenses[40] and holograms,[41,42] we use a single metasurface to engineer the singularity structures of CVBs through the superposition of multiple vortex beams. We have shown that the phase singularities can be tailored by controlling initial phases, amplitude coefficients, and incident polarization states of the LG modes with different topological charges. The change of singularity structures leads to the change of the spatial intensity distributions, which have potential applications in particle manipulation, optical communications, and electromagnetically induced transparency. Moreover, vortex beam detection is crucial for practical applications.[43,44] It has been shown by Guo et al. that a spin decoupled metasurface can simultaneously detect spin and phase singularities,[43] which can be used to analyze the components of the generated CVBs.

Although the metasurface is designed at 630 nm, it can also work at other wavelengths due to the broadband nature of the geometric metasurface. The experimental results for the superposition of $LG_1 + LG_5 + LG_{20} + LG_{-20}$ at other wavelengths are provided in Section S7 (Supporting Information). The measured diffraction efficiency for the superposition of four vortex beams at 630 nm is about 7%. The diffraction efficiency at other wavelengths is provided in Section S8 (Supporting Information). The simulation results with and
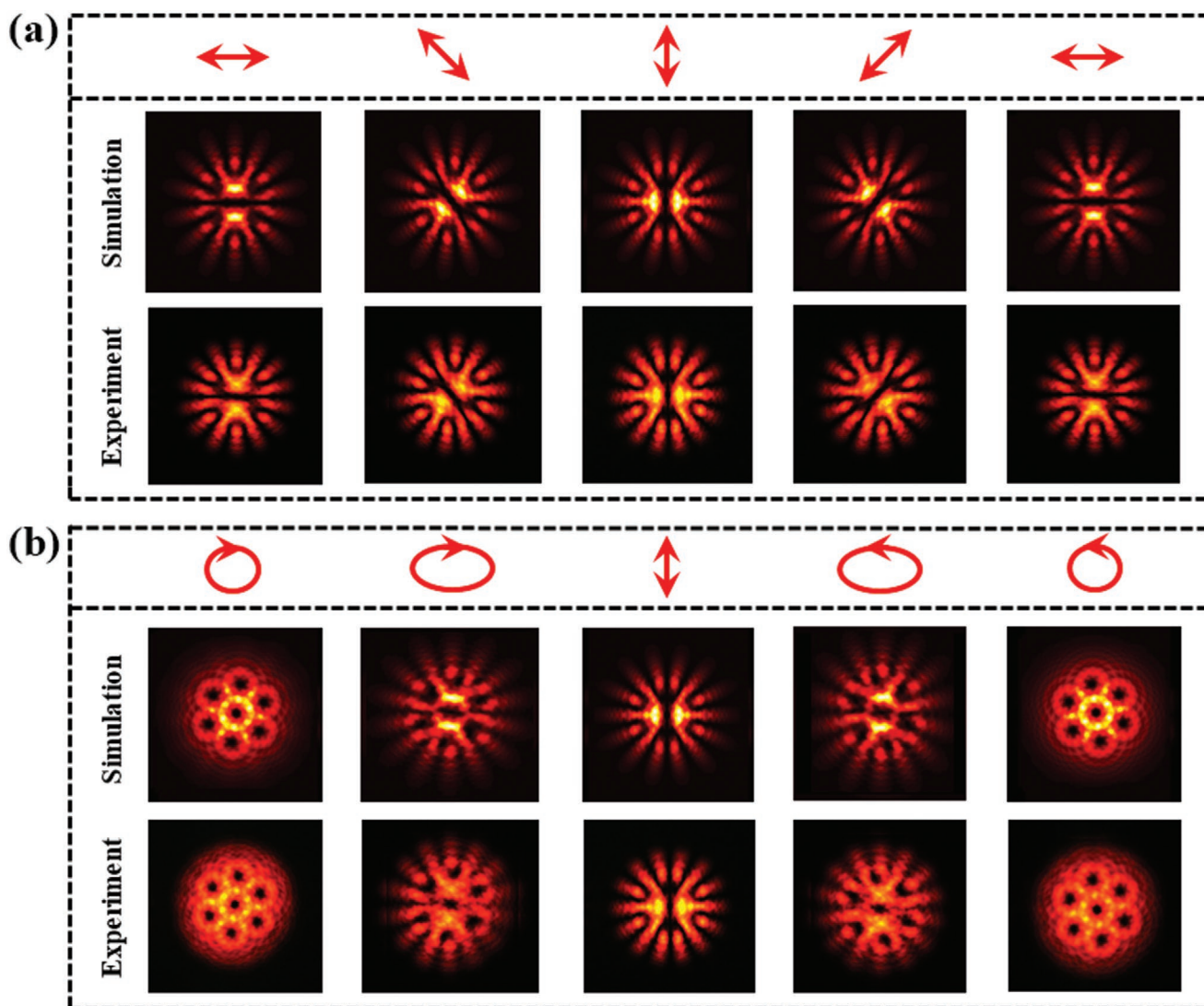
Figure 5. CVBs generation based on the superposition of four LG modes with different circular polarization states. The polarization state of input light plays an important role in the resultant CVBs. a) Intensity patterns of the CVBs after passing through an analyser (linear polarizer) with a fixed transmission axis (vertical direction). The transmission axes of the first linear polarizer are denoted by the red double arrows. The quarter wave plate is removed here. b) Effect of the polarization state on the intensity patterns. The fast axis of the quarter wave plate and the transmission axis of the analyser are along the horizontal and vertical directions, respectively. To change the polarization state of the incident light, the transmission axis of the first linear polarizer is rotated.

without considering the complex amplitude information are compared in Section S9 (Supporting Information). Although the results look slightly different by considering the complex amplitude modulation, it is a big challenge for nanofabrication since nanostructures with different feature sizes are needed. From the practical point of view, it is more convenient to prepare phase-only metasurfaces, which may bring the CVBs one step closer to real-world applications. The good agreement between simulation and experimental results has showed that our metasurface design is very robust against fabrication errors.

Although the design process for the superposition of more than four vortex beams is the same, there are some restrictions in both the numerical optimization process and sample fabrication. The maximum number of vortex beams is mainly

determined by the sample size and the design parameters of metasurfaces (e.g., pixel size). For example, the increase of pixel number and the reduction of pixel size of the metasurface can increase the number of vortex beams. The zero-order beam could be reduced by using dielectric metasurfaces (instead of metallic nanostructures) with higher transmission efficiencies, which would allow the off-axis design to be carried out on-axis.

Our metasurface approach has several advantages over conventional methods for generating composite vortex beams. First, our work has overcome various practical and technical challenges in conventional methods for the realization of vortex beam superpositions, such as bulky experimental setup, misalignment and phase aberration. A single metasurface device can perform the superposition of multiple vortex beams with different circular polarization states, which is very challenging

or impossible with conventional optics that requires a cascade of many bulky optical elements and alignment systems. Second, our metasurface design is very robust against fabrication errors and provides a unique tool for creating and investigating composite vortex beams. Finally, the capability to generate composite vortex beams with engineered singularity distributions with a minimal footprint paves a new avenue for highly compact metadevices in singular optics and quantum science.

4. Conclusion

We experimentally demonstrate the creation of CVBs based on a single metasurface through the superposition of multiple LG modes. Different CVBs are obtained by controlling the initial phases, amplitude coefficients, and incident polarization states. Our method provides a compact platform to generate CVBs without a complicated optical system, which can further facilitate integrated photonics. The ultrathin nature, subwavelength resolution, and superposition of multiple OAM beams make this technology very attractive for potential applications ranging from particle manipulation and electromagnetically induced transparency to quantum computation gate.

5. Experimental Section

Sample Fabrication: The geometric metasurfaces consist of gold nanorods with spatially variant orientations sitting an ITO coated glass substrate. First, the substrates are cleaned with acetone for 10 min in an ultrasonic bath, followed by isopropyl alcohol (IPA) for 10 min. Then, the poly(methyl methacrylate) (PMMA) 950 A2 resist is spin-coated on the substrates at 1000 rpm for 60 s, which can produce a resist film (100 nm thick). After that, the samples are baked on a hotplate at 180 °C for 5 min. The electron beam lithography (Raith PIONEER, 30 kV) was used to define nanopatterns. The samples were developed in MIBK:IPA (1:3) for 45 s and rinsed IPA for 45 s. An electron beam evaporator was used to deposit a 40 nm-thick gold film on the samples. Finally, the metasurfaces were ready for characterization after the lift-off process.

Supporting Information

Supporting Information is available from the Wiley Online Library or from the author.

Acknowledgements

Conflict of Interest

The authors declare no conflict of interest.

Data Availability Statement

The data that support the findings of this study are available from the corresponding author upon reasonable request.

[1] M. R. Dennis, K. O'Holleran, M. J. Padgett, *Prog. Opt.* **2009**, *53*, 293.
[2] V. G. Shvedov, A. V. Rode, Y. V. Izdebskaya, A. S. Desyatnikov, W. Krolikowski, Y. S. Kivshar, *Phys. Rev. Lett.* **2010**, *105*, 118103.
[3] T. Chantakit, C. Schlickriede, B. Sain, F. Meyer, T. Weiss, N. Chattham, T. Zentgraf, *Photonics Res.* **2020**, *8*, 1435.
[4] E. Nagali, F. Sciarrino, F. de Martini, L. Marrucci, B. Piccirillo, E. Karimi, E. Santamato, *Phys. Rev. Lett.* **2009**, *103*, 013601.
[5] Y. Ming, W. Zhang, J. Tang, Y. Liu, Z. Xia, Y. Liu, Y.-Q. Lu, *Laser Photonics Rev.* **2020**, *14*, 1900146.
[6] A. M. Yao, M. J. Padgett, *Adv. Opt. Photonics* **2011**, *3*, 161.
[7] S. Huang, Z. Miao, C. He, F. Pang, Y. Li, T. Wang, *Opt. Lasers Eng.* **2016**, *78*, 132.
[8] I. D. Maleev, G. A. SwartzlanderJr., *J. Opt. Soc. Am. B* **2003**, *20*, 1169.
[9] Y. Tian, L. Wang, G. Duan, L. Yu, *Opt. Commun.* **2021**, *485*, 126712.
[10] H. R. Hamedi, V. Kudriašov, N. Jia, J. Qian, G. Juzeliūnas, *Opt. Lett.* **2021**, *46*, 4204.
[11] V. E. Lembessis, A. Lyras, O. M. Aldossary, *J. Opt. Soc. Am. B* **2021**, *38*, 233.
[12] M. Szatkowski, J. Masajada, I. Augustyniak, K. Nowacka, *Opt. Commun.* **2020**, *463*, 125341.
[13] X. Chen, L. Huang, H. Mühlenbernd, G. Li, B. Bai, Q. Tan, G. Jin, C.-W. Qiu, S. Zhang, T. Zentgraf, *Nat. Commun.* **2012**, *3*, 1198.
[14] W. T. Chen, A. Y. Zhu, V. Sanjeev, M. Khorasaninejad, Z. Shi, E. Lee, F. Capasso, *Nat. Nanotechnol.* **2018**, *13*, 220.
[15] S. Wang, P. C. Wu, V.-C. Su, Y.-C. Lai, M.-K. Chen, H. Y. Kuo, B. H. Chen, Y. H. Chen, T.-T. Huang, J.-H. Wang, R.-M. Lin, C.-H. Kuan, T. Li, Z. Wang, S. Zhu, D. P. Tsai, *Nat. Nanotechnol.* **2018**, *13*, 227.
[16] R. Wang, Y. Intaravanne, S. Li, J. Han, S. Chen, J. Liu, S. Zhang, L. Li, X. Chen, *Nano Lett.* **2021**, *21*, 2081.
[17] P. Genevet, F. Capasso, F. Aieta, M. Khorasaninejad, R. Devlin, *Optica* **2017**, *4*, 139.
[18] X. Chen, Y. Luo, J. Zhang, K. Jiang, J. B. Pendry, S. Zhang, *Nat. Commun.* **2011**, *2*, 176.
[19] A. Arbabi, E. Arbabi, S. M. Kamali, Y. Horie, S. Han, A. Faraon, *Nat. Commun.* **2016**, *7*, 13682.
[20] Z. Li, Q. Dai, M. Q. Mehmood, G. Hu, B. Luk'yanchuk, J. Tao, C. Hao, I. Kim, H. Jeong, G. Zheng, S. Yu, A. Alù, J. Rho, C.-W. Qiu, *Light: Sci. Appl.* **2018**, *7*, 63.
[21] A. M. Shaltout, J. Kim, A. Boltasseva, V. M. Shalaev, A. V. Kildishev, *Nat. Commun.* **2018**, *9*, 2673.

[22] P. Genevet, F. Capasso, *Rep. Prog. Phys.* **2015**, *78*, 024401.

[23] E. Arbabi, S. M. Kamali, A. Arbabi, A. Faraon, *ACS Photonics* **2019**, *6*, 2712.

[24] Z.-L. Deng, M. Jin, X. Ye, S. Wang, T. Shi, J. Deng, N. Mao, Y. Cao, B. O. Guan, A. Alù, *Adv. Funct. Mater.* **2020**, *30*, 1910610.

[25] I. Kim, J. Jang, G. Kim, J. Lee, T. Badloe, J. Mun, J. Rho, *Nat. Commun.* **2021**, *12*, 3614.

[26] L. Huang, X. Chen, H. Müehlenbernd, G. Li, B. Bai, Q. Tan, G. Jin, T. Zentgraf, S. Zhang, *Nano Lett.* **2012**, *12*, 5750.

[27] F. Yue, D. Wen, J. Xin, B. D. Gerardot, J. Li, X. Chen, *ACS Photonics* **2016**, *3*, 1558.

[28] Y. Chen, X. Yang, J. Gao, *Adv. Opt. Mater.* **2018**, *6*, 1800646.

[29] Q. Dai, Z. Li, L. Deng, N. Zhou, J. Deng, J. Tao, G. Zheng, *Opt. Lett.* **2020**, *45*, 3773.

[30] Y. Ming, W. Zhang, J. Tang, X. Yang, Y.-S. Liu, Y.-Q. Lu, *ACS Photonics* **2021**, *8*, 1896.

[31] J. Li, S. Chen, H. Yang, J. Li, P. Yu, H. Cheng, C. Gu, H. T. Chen, J. Tian, *Adv. Funct. Mater.* **2015**, *25*, 704.

[32] J. Kim, S. Choudhury, C. DeVault, Y. Zhao, A. V. Kildishev, V. M. Shalaev, A. Alu, A. Boltasseva, *ACS Nano* **2016**, *10*, 9326.

[33] J. Y. Guo, X. K. Wang, J. W. He, H. Zhao, S. F. Feng, P. Han, J. S. Ye, W. F. Sun, G. H. Situ, Y. Zhang, *Adv. Opt. Mater.* **2018**, *6*, 1700925.

[34] F. Yue, D. Wen, C. Zhang, B. D. Gerardot, W. Wang, S. Zhang, X. Chen, *Adv. Mater.* **2017**, *29*, 1603838.

[35] Y. Zhang, X. Zeng, L. Ma, R. Zhang, Z. Zhan, C. Chen, X. Ren, C. He, C. Liu, C. Cheng, *Adv. Opt. Mater.* **2019**, *7*, 1900372.

[36] C. Zheng, G. Wang, J. Li, J. Li, S. Wang, H. Zhao, M. Li, Z. Yue, Y. Zhang, Y. Zhang, J. Yao, *Adv. Opt. Mater.* **2021**, *9*, 2002007.

[37] S. Baumann, D. Kalb, L. MacMillan, E. Galvez, *Opt. Express* **2009**, *17*, 9818.

[38] Q. Jiang, G. Jin, L. Cao, *Adv. Opt. Photonics* **2019**, *11*, 518.

[39] X. Luo, X. Li, M. Pu, Y. Guo, F. Zhang, X. Ma, *Prog. Quantum Electron.* **2021**, *79*, 100344.

[40] F. Zhang, M. Pu, X. Li, X. Ma, Y. Guo, P. Gao, H. Yu, M. Gu, X. Luo, *Adv. Mater.* **2021**, *33*, 2008157.

[41] X. Zhang, M. Pu, Y. Guo, J. Jin, X. Li, X. Ma, J. Luo, C. Wang, X. Luo, *Adv. Funct. Mater.* **2019**, *29*, 1809145.

[42] M. A. Ansari, T. Tauqeer, M. Zubair, M. Q. Mehmood, *Nanophotonics* **2020**, *9*, 963.

[43] Y. Guo, S. Zhang, M. Pu, Q. He, J. Jin, M. Xu, Y. Zhang, P. Gao, X. Luo, *Light: Sci. Appl.* **2021**, *10*, 63.

[44] J. A. Anguita, J. Herreros, J. E. Cisternas, *CLEO: Sci. Innovations* **2012**, JTu2K.5.